nature nanotechnology

SUPPLEMENTARY INFORMATION

https://doi.org/10.1038/s41565-019-0486-y

In the format provided by the authors and unedited.

Theoretical strength and rubber-like behaviour in micro-sized pyrolytic carbon

Xuan Zhang[1,4], Lei Zhong[1,4], Arturo Mateos[2,4], Akira Kudo[2], Andrey Vyatskikh[2], Huajian Gao[3*], Julia R. Greer[2*] and Xiaoyan Li[1*]

[1]Centre for Advanced Mechanics and Materials, Applied Mechanics Laboratory, Department of Engineering Mechanics, Tsinghua University, Beijing, China. [2]Division of Engineering and Applied Science, California Institute of Technology, Pasadena, CA, USA. [3]School of Engineering, Brown University, Providence, RI, USA. [4]These authors contributed equally: Xuan Zhang, Lei Zhong, Arturo Mateos. *e-mail: Huajian_Gao@brown.edu; jrgreer@caltech.edu; xiaoyanlithu@tsinghua.edu.cn

Supplementary Text 1. Influence of the residual carbon ring on the strength

To eliminate possible influence of the residual carbon ring (Fig. 2b), we used focused ion beam milling to remove the ring from the samples (Fig. 2c and Supplementary Fig. 7d before compression). Supplementary Figure 9 shows the compressive deformation of a 1.86-μm-diameter micropillar that retained the residual carbon ring, which bulged and detached from the substrate during compression and led to a substantial strain burst at a strain of ~36%, as shown in Supplementary Fig. 9d. The maximum attained stresses in Supplementary Fig. 9d are comparable to those in Fig. 2c and Supplementary Fig. 7d, which implies a marginal contribution of the residual carbon ring to the strength.

Supplementary Text 2. Hysteresis of micropillars with D<2.3 μm

To quantify the hysteresis of micropillars with D<2.3 μm (Supplementary Fig. 10 and 11), we calculated the dissipated energy per unit volume of our micropillars by integrating the area enclosed by loading and unloading curves, and then plotted it versus Young's modulus along with the corresponding properties of some conventional engineering materials, as well as Au-nanowires (Au-NWs)[10], Cu nanopillars (Cu-NPs)[37], SU-8 composites[44] and bulk metallic glasses[S1] in Supplementary Fig. 12. It can be seen from this plot that pyrolytic carbon micropillars exhibit 1-3 orders of magnitude higher energy dissipation than many bulk or nanoscale structural materials[10,37,44,S1] with comparable Young's modulus. The origin of the hysteresis could be related to the re-arrangement of graphene fragments and the interlayer shear/friction between neighboring graphene layers (illustrated by Figs. 4d-4g from our subsequent atomistic simulations), which could lead to differences in local stresses and strains during loading vs. unloading.

Supplementary Text 3. Discussions about compressive strength of micropillars with D<2.3 μm and tension-compression asymmetry

We observed in Fig. 3b that the compressive strengths of the micropillars with D<2.3 μm have a significant fluctuation. Such fluctuation could arise from variations in the length of the initial splitting microcrack h, as indicated by Eq. (2) in the main text. Previous experimental studies[S2-S5] have reported that various defects, such as non-six membered rings, pores, voids and cracks, can emerge during pyrolysis of polymers as a result of carbonization and release of volatiles. It seems that the initial splitting cracks in our samples were indeed generated during the pyrolysis. Their formation might be due to structural re-configurations or aggregation of defects during pyrolysis. The average compressive strengths of the micropillars with D<2.3 μm are higher by a factor of 4.8 than the corresponding average tensile strengths of 1.6 GPa. This tension-compression asymmetry is close to the theoretical prediction of an asymmetry factor of 2.5-4.4 that arises in high-strength, covalently bonded isotropic materials, as determined from a fracture criterion[S6].

Supplementary Text 4. Influence of initial crack on the strength of pyrolytic carbon pillars

Figure 4c shows that the tensile strength of a nanopillar without initial cracks is above 20 GPa, which stems from the large forces required to break covalent bonds. This strength is reduced to approximately 12 GPa after introducing cracks into the nanopillar, indicating that the presence of initial flaws/imperfections can cause significant reduction in tensile strength. Supplementary Figure 15 shows the deformation processes of nanopillars with initial 4- and 8 nm-long nanocracks. We observed that their failure always originated from the growth and extension of pre-existing nanocracks, leading to a smaller fracture strain and a smoother fracture surface than in nanopillars without nanocracks. The tensile strengths of the simulated samples are much higher than those of the experimental samples, which is a common phenomenon caused by a difference of 10-11 orders of magnitude in the applied strain rate, as well as a difference of 1-2 orders of magnitude in sample size and non-equivalent flaw concentrations in the experiments and simulations.

Supplementary Text 5. Differences in mechanical properties between pyrolytic carbon micropillars and existing pyrolytic carbon

It is noted that our pyrolytic carbon micropillars exhibit 1.5-8.2 times higher compressive strength and at least one order of magnitude larger fracture strain than existing bulk and millimeter-sized pyrolytic carbon[23,25]. These differences in mechanical properties can be attributed to differences in microstructures and sample sizes between materials. First, the crystallite size of the carbon layer fragments in our pyrolytic carbon are much smaller than those (about 4-6 nm) of the existing bulk and millimeter -sized pyrolytic carbon[23,25]. These different microstructures are induced by different pyrolysis precursor materials and conditions (such as temperature and duration time). Second, our pyrolytic carbon with high strength and large deformability are several microns in diameters, which are 2-4 orders of magnitude smaller than diameters (beyond hundreds of microns) of bulk and millimeter-sized pyrolytic carbon[23,25]. Therefore, designing/controlling atomic-level microstructures and sample dimension have resulted in significant enhancement of the mechanical properties of pyrolytic carbon.

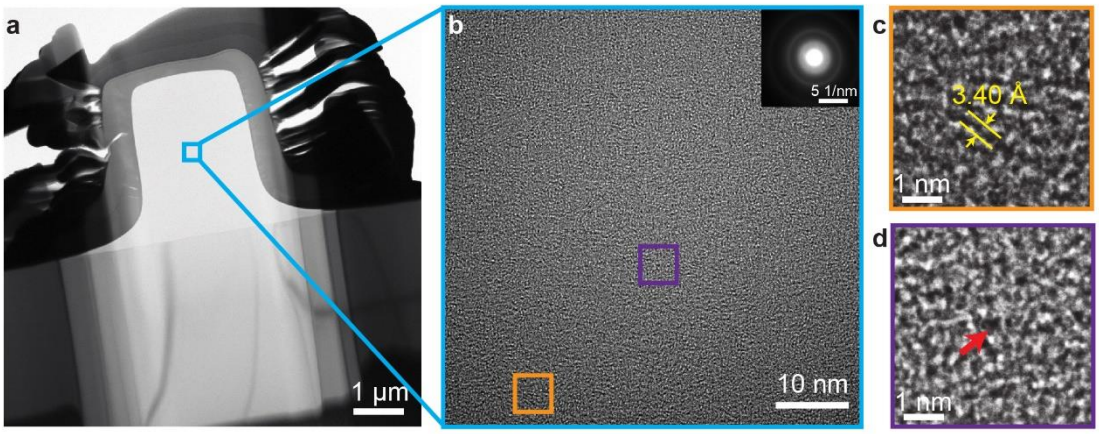

Supplementary Fig. 1 | TEM samples extracted from pyrolytic carbon micropillar with diameter of 2.3 μm by FIB and their HRTEM images. a, TEM sample prepared by FIB milling. **b**, Zoomed-in TEM image of a boxed region in a. **c**, **d**, HRTEM images of the two regions outlined by solid boxes in b. A typical sub-nanometer-sized void is pointed by a red arrow.

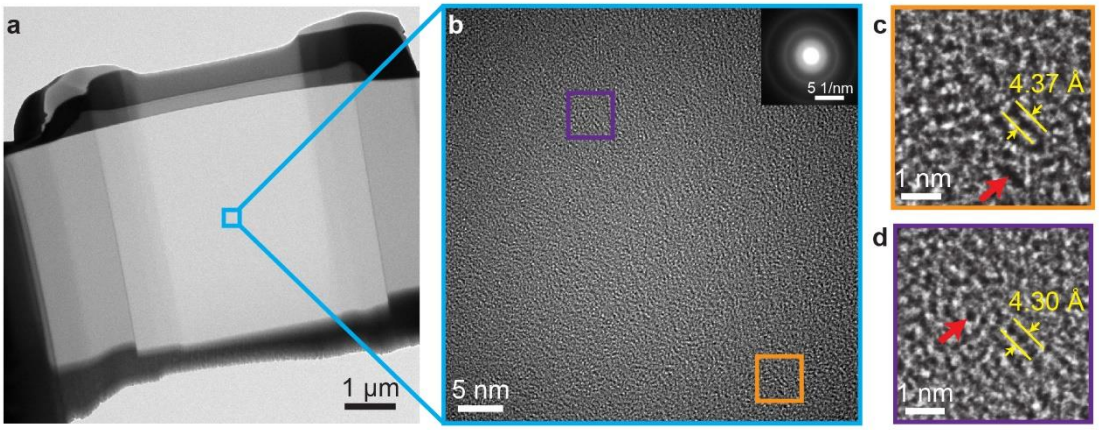

Supplementary Fig. 2 | TEM samples extracted from pyrolytic carbon micropillar with diameter of 12.7 μm by FIB and their HRTEM images. a, TEM sample prepared by FIB milling. **b**, Zoomed-in TEM image of a boxed region in a. **c**, **d**, HRTEM images of the two regions outlined by solid boxes in b. Several sub-nanometer-sized voids are pointed by red arrows.

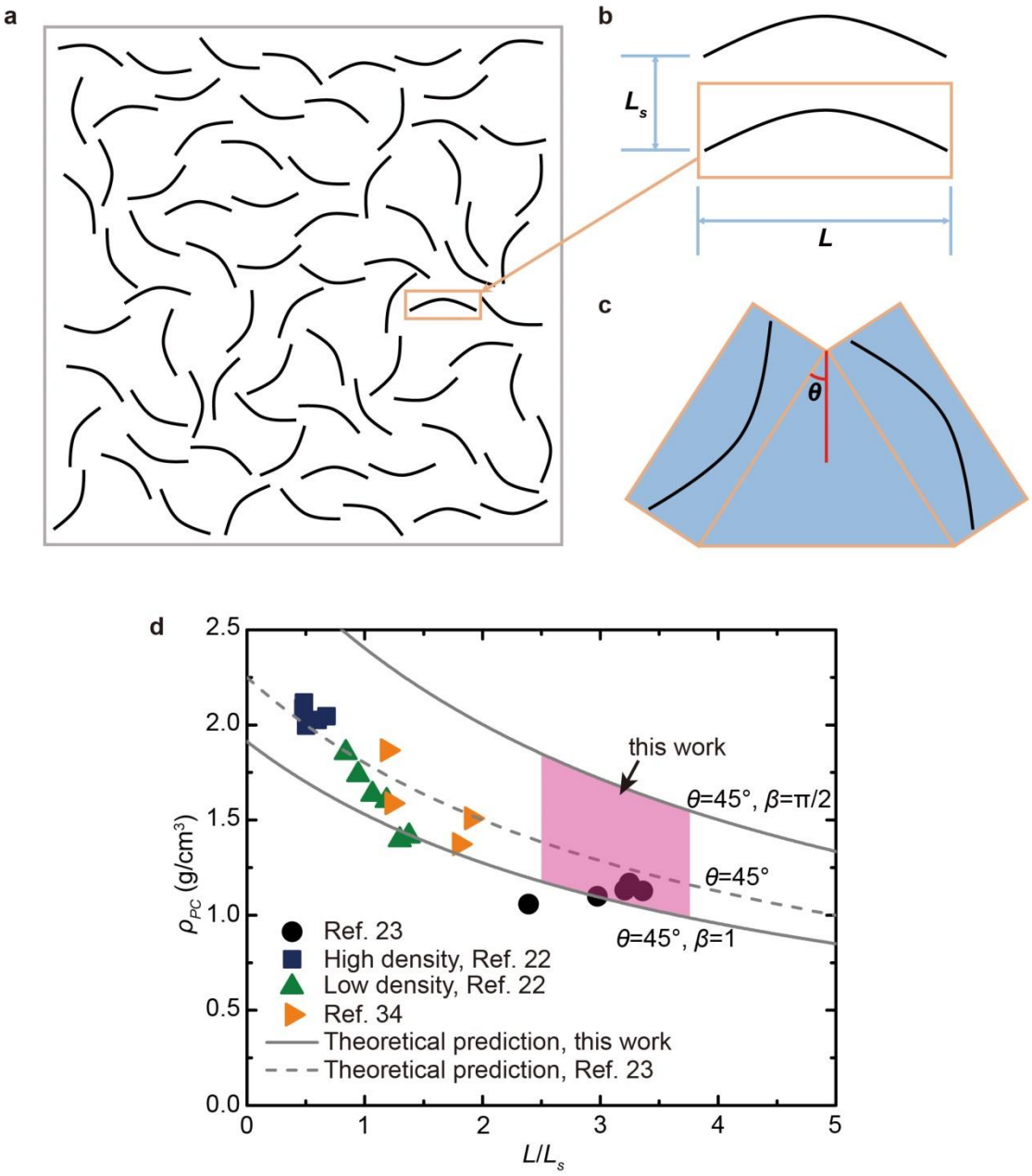

Supplementary Fig. 3 | Model for density estimation of pyrolytic carbon and comparison with densities reported in recent literatures. a, **b**, Illustration of packing structure of curved graphene layers in pyrolytic carbon. *L* is the size of curved graphene layer, and L_s represents the interlayer distance between neighboring layers. **c**, Illustration of a typical open-structure unit cell composed of two graphene layers. **d**, Density of pyrolytic carbon (ρ_{PC}) as a function of the ratio of L/L_s. Solid curve is from the prediction based on Eq. (4) in Methods, while the dashed curve is from Ref. 23. The current extended model supplies a prediction of density of 1.0-1.8 g/cm^3 for pyrolytic carbon micropillars.

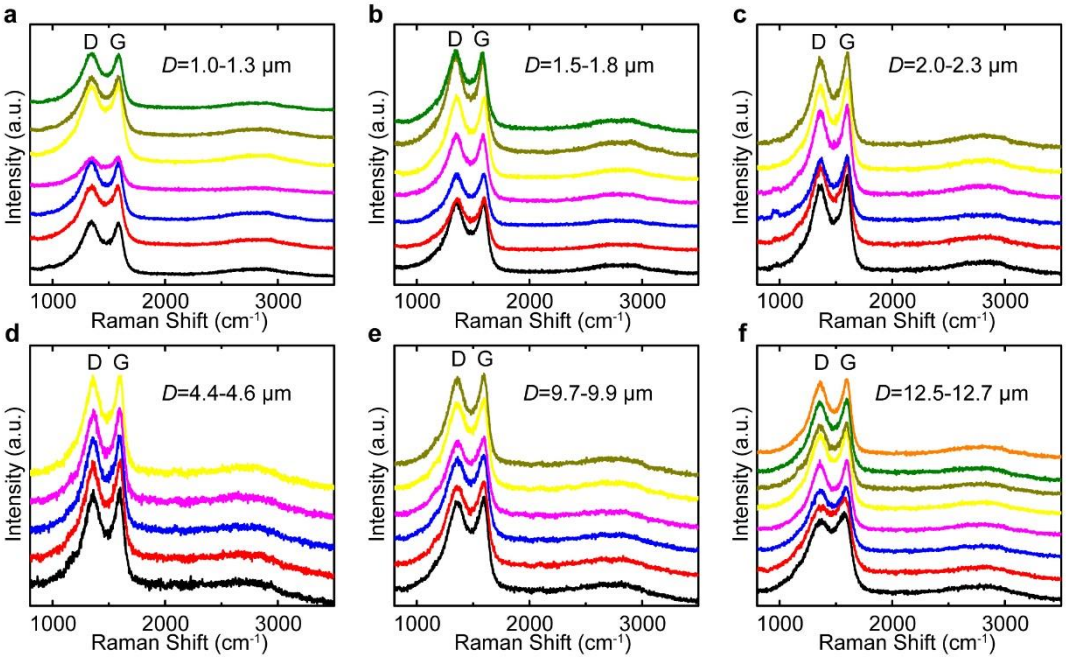

Supplementary Fig. 4 | Raman spectra measured on samples with diameters of 1.0-12.7 μm. All spectra contain two prominent peaks at Raman shifts of ~1359 cm^{-1} (*D*-peak) and ~1595 cm^{-1} (*G*-peak), respectively.

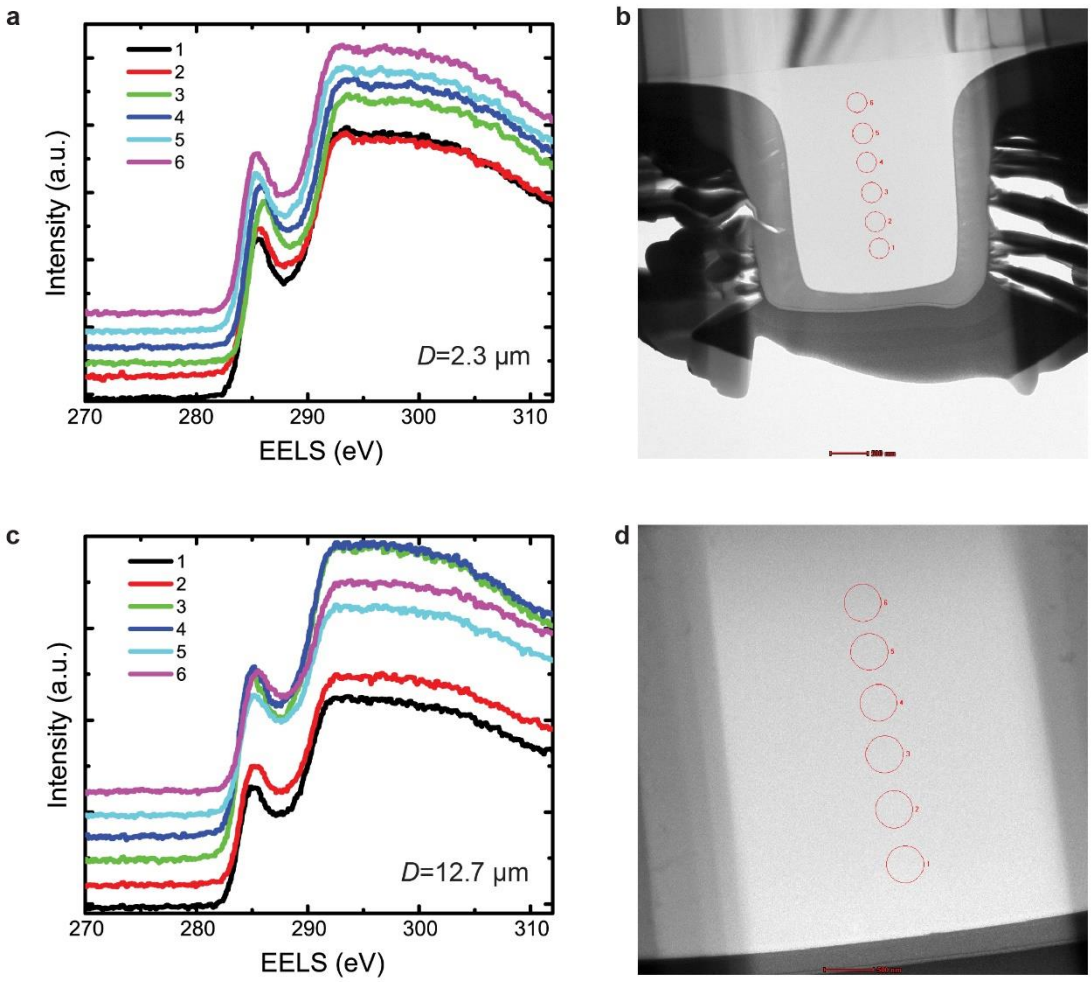

Supplementary Fig. 5 | EELS spectra on two TEM samples extracted from pyrolytic carbon micropillars. a, EELS spectra on TEM sample from micropillar with diameter of 2.3 μm. **b**, TEM image of FIB-cut sample from micropillar with diameter of 2.3 μm. **c**, EELS spectra on TEM sample from micropillar with diameter of 12.7 μm. **d**, TEM image of FIB-cut sample from micropillar with diameter of 12.7 μm. The labels in a and c correspond to the circled sites in b and d, respectively.

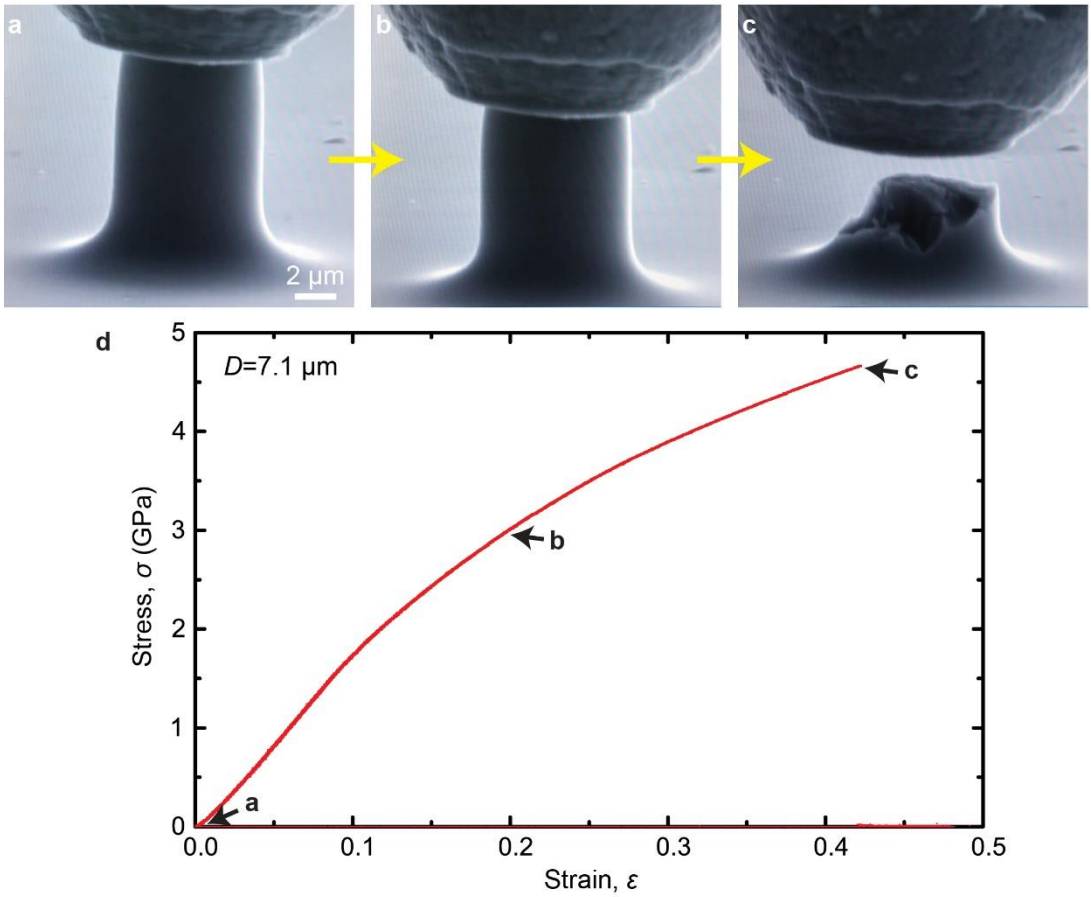

Supplementary Fig. 6 | In situ compression experiment of pyrolytic carbon micropillar with diameter of 7.1 μm. a-c, Snapshots from in situ compressive test on the micropillar. **d**, Stress-strain curve of tested sample. The labels in d correspond to the labels in a-c. The sample underwent catastrophic fracture at the maximum applied stress.

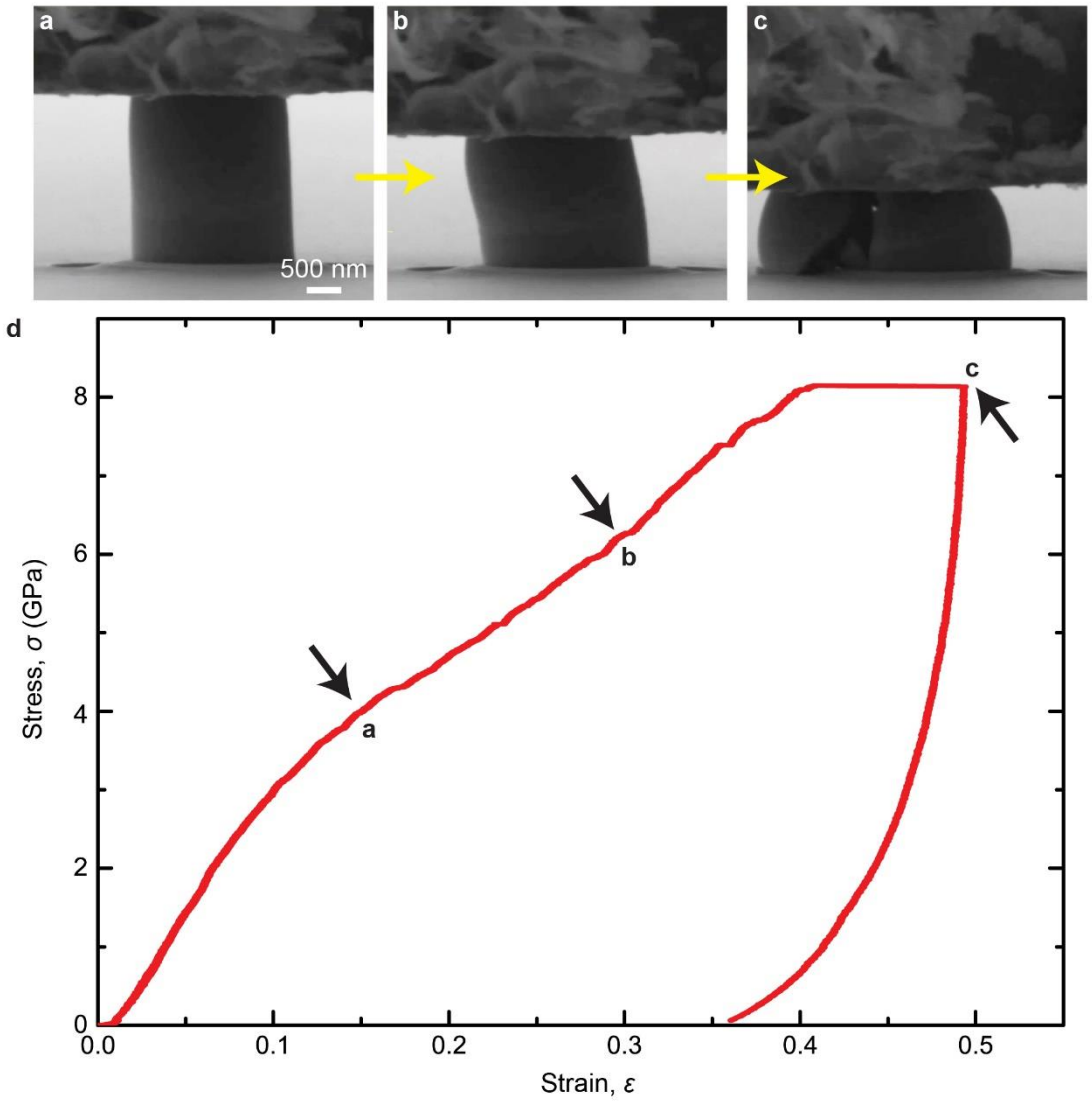

Supplementary Fig. 7 | In situ compression experiment of pyrolytic carbon micropillar without the residual ring. a-c, Snapshots of in situ compressive test on a pyrolytic carbon pillar without the residual ring. In **c**, a splitting crack nucleated and propagated rapidly under high compressive stress, leading to catastrophic fracture of the micropillar. **d**, Corresponding compressive stress-strain curve.

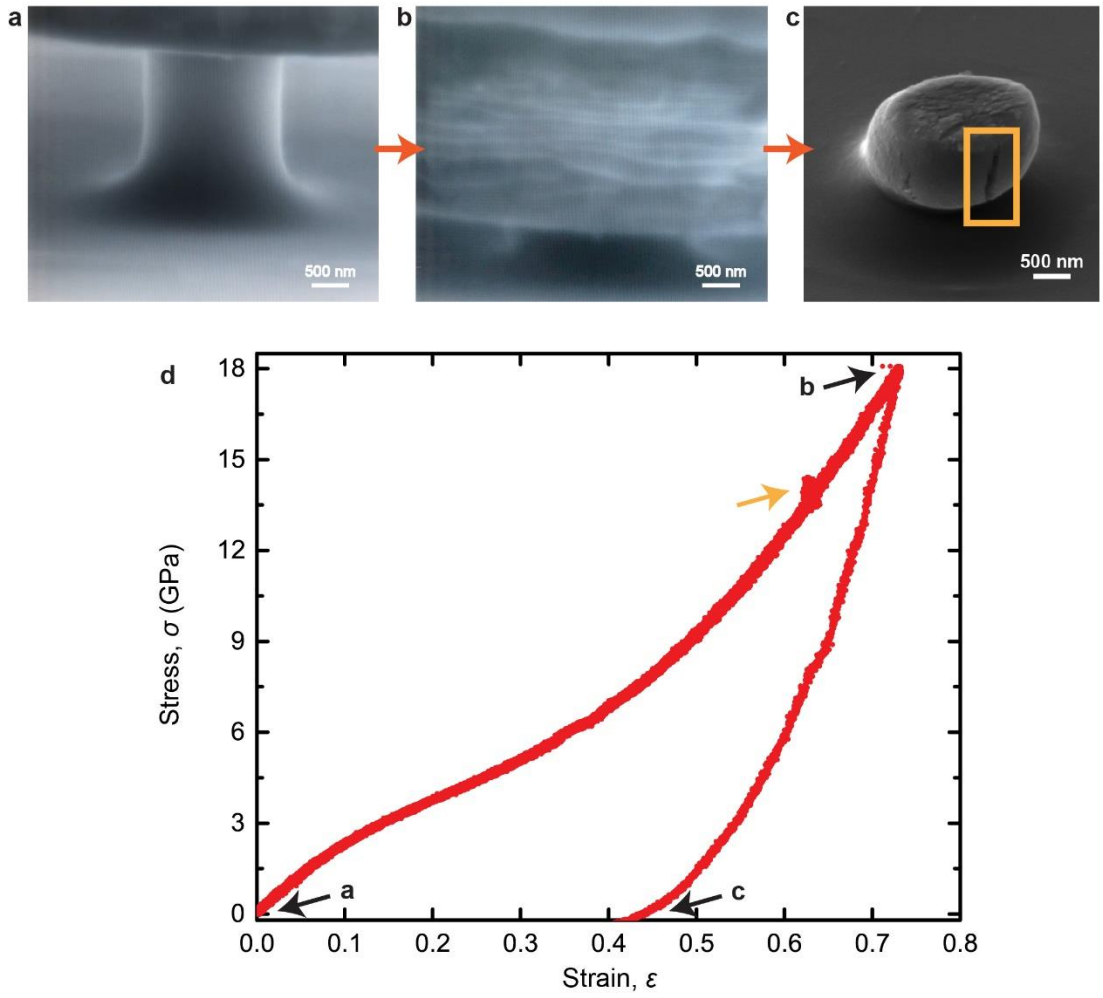

Supplementary Fig. 8 | In situ compression experiment of a pyrolytic carbon micropillar with diameter of 1.8 μm. a-c, Snapshots from in situ compressive test on the micropillar. A splitting microcrack (boxed in c) in the sample after compression. **d**, Stress-strain curve of the tested sample. The labels in d correspond to those in a-c. Microcrack likely nucleated at a high stress-level, leading to an apparent stress fluctuation indicated by the orange arrow in d. The stress at the first fluctuation is identified as the compressive strength of such sample.

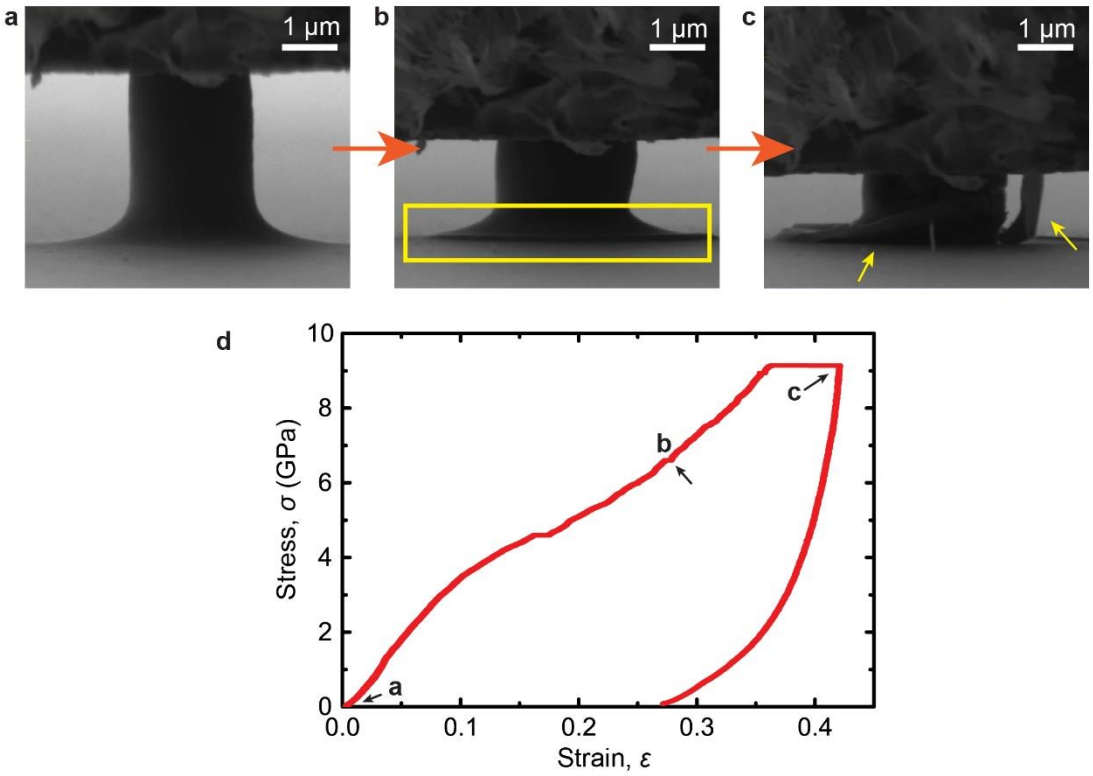

Supplementary Fig. 9 | Influence of residual carbon rings on compression of pyrolytic carbon micropillars. a-c, Snapshots of in situ compressive test on a pyrolytic carbon pillar with the residual ring. **d**, Corresponding compressive stress-strain curve. The slight burst marked by **b** is corresponding to the bulging of the edge of the ring due to high stress concentration. The large strain burst marked by **c** represents cleavage of the pillar as well as peeling up of the ring.

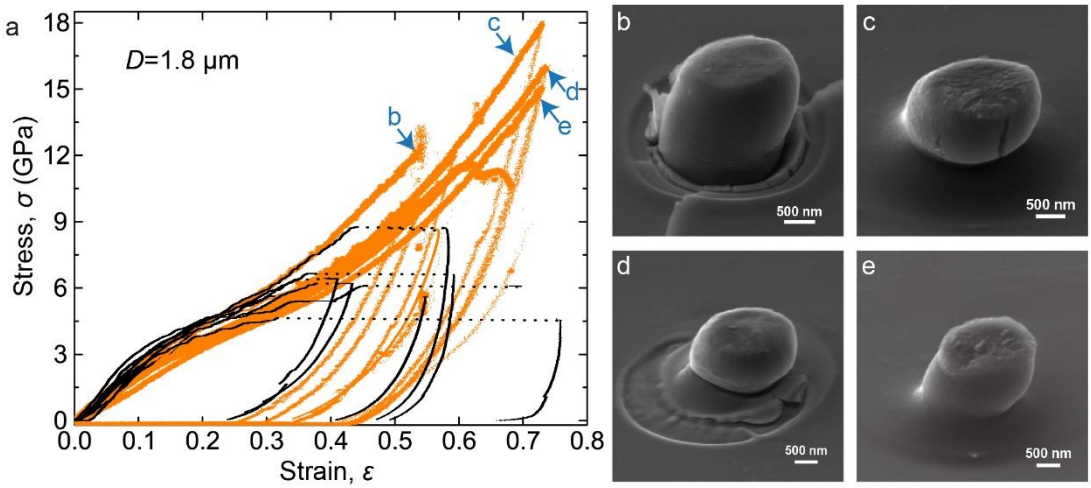

Supplementary Fig. 10 | Mechanical responses and post-deform SEM images of compressed micropillars with diameter of 1.8 μm. a, Compressive stress-strain curves of all tested micropillars with diameter of 1.8 μm. In a, the dotted lines are used to connect the intermittent data points from the testing. **b-e**, SEM images of 4 samples labeled in a after compression.

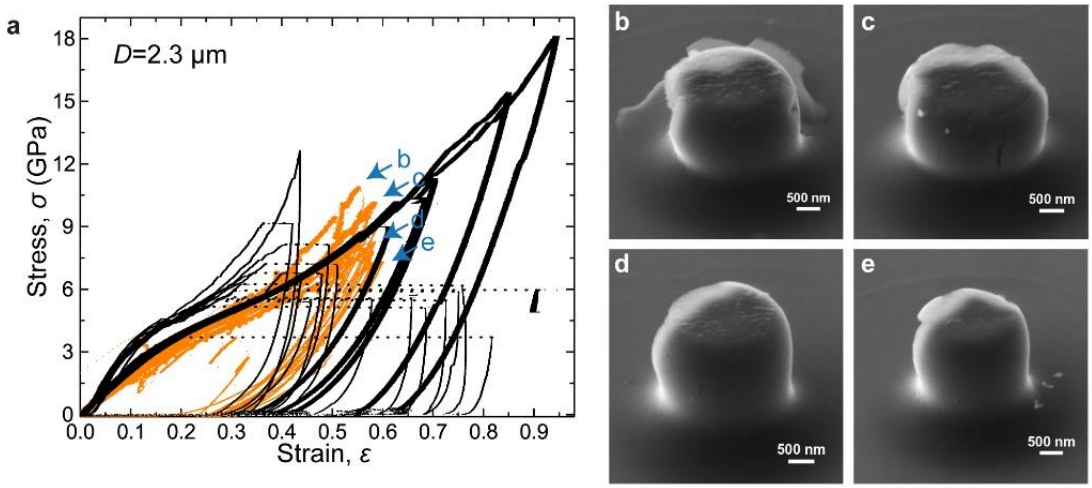

Supplementary Fig. 11 | Mechanical responses and post-deform SEM images of compressed micropillars with diameter of 2.3 μm. a, Compressive stress-strain curves of all tested micropillars with diameter of 2.3 μm. In **a**, the dotted lines are used to connect the intermittent data points from the testing. **b-e,** SEM images of 4 samples labeled in **a** after compression.

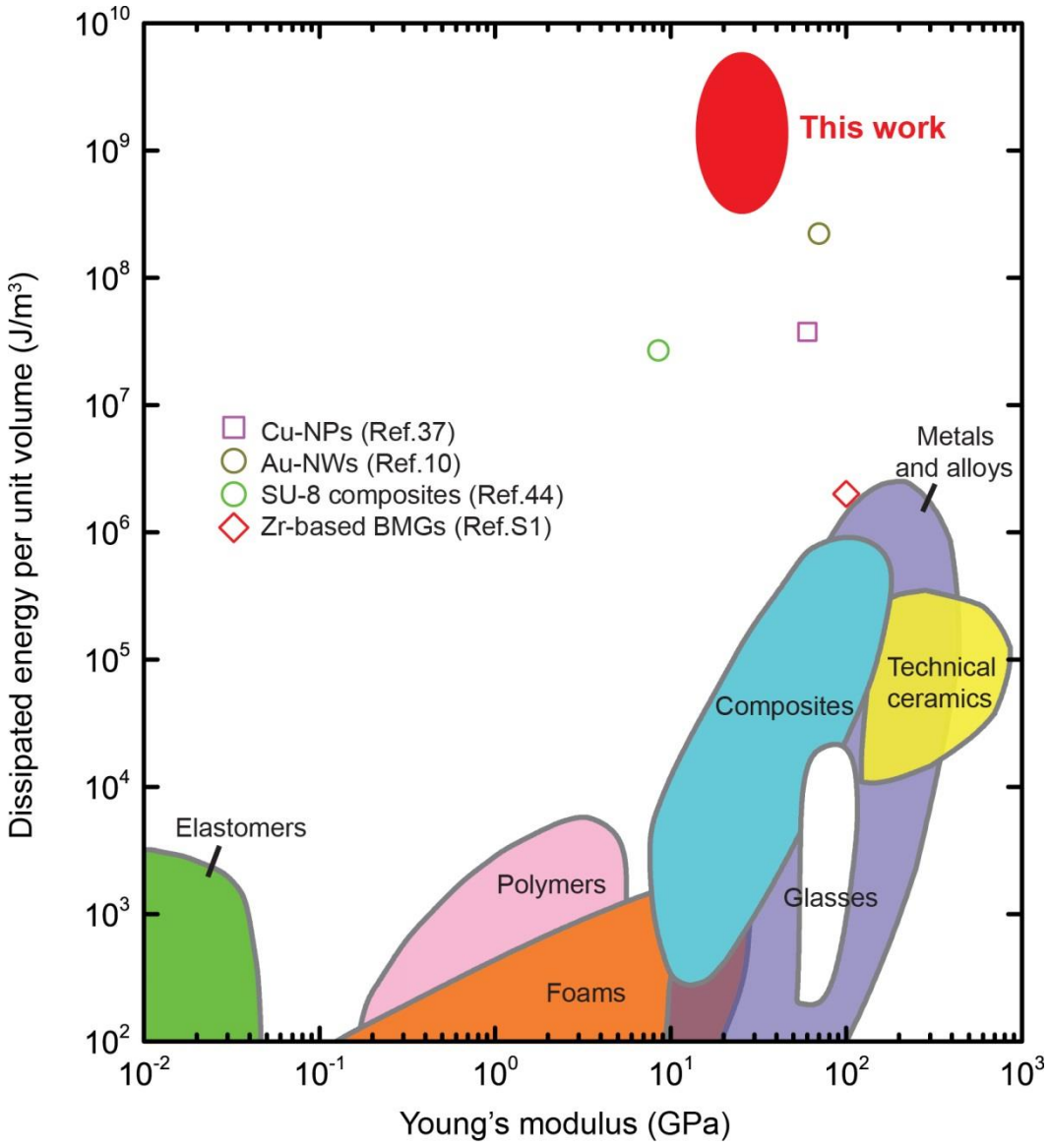

Supplementary Fig. 12 | Dissipated energy per unit volume vs. Young's modulus diagram of our pyrolytic carbon micropillars and other structural materials. We compared our pyrolytic carbon micropillars with various structural materials, including some conventional engineering materials, Au-NWs[10], Cu-NPs[37], SU-8 composites[44] and bulk metallic glasses[S1].

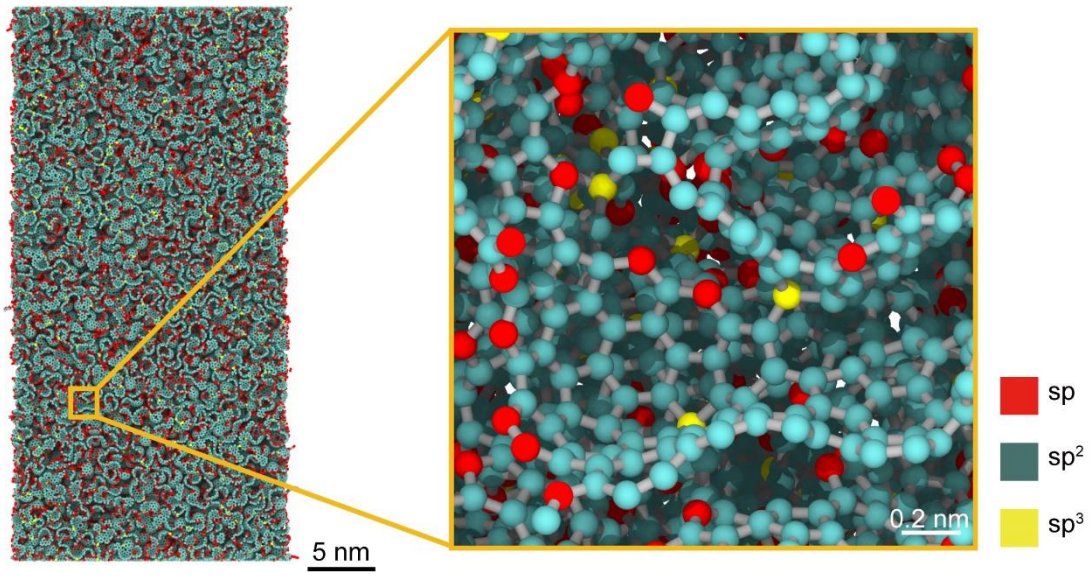

Supplementary Fig. 13 | Bonding structures of pyrolytic carbon pillars used for atomistic simulations. Note that the sp^2 bonds are much more ubiquitous than sp and sp^3 bonds. The sp bonds are mainly localized at the edges of the curved graphene layers; the sp^3 bonds generally connect neighboring graphene layers to one another or form at some high-energy curved surface of graphene layers.

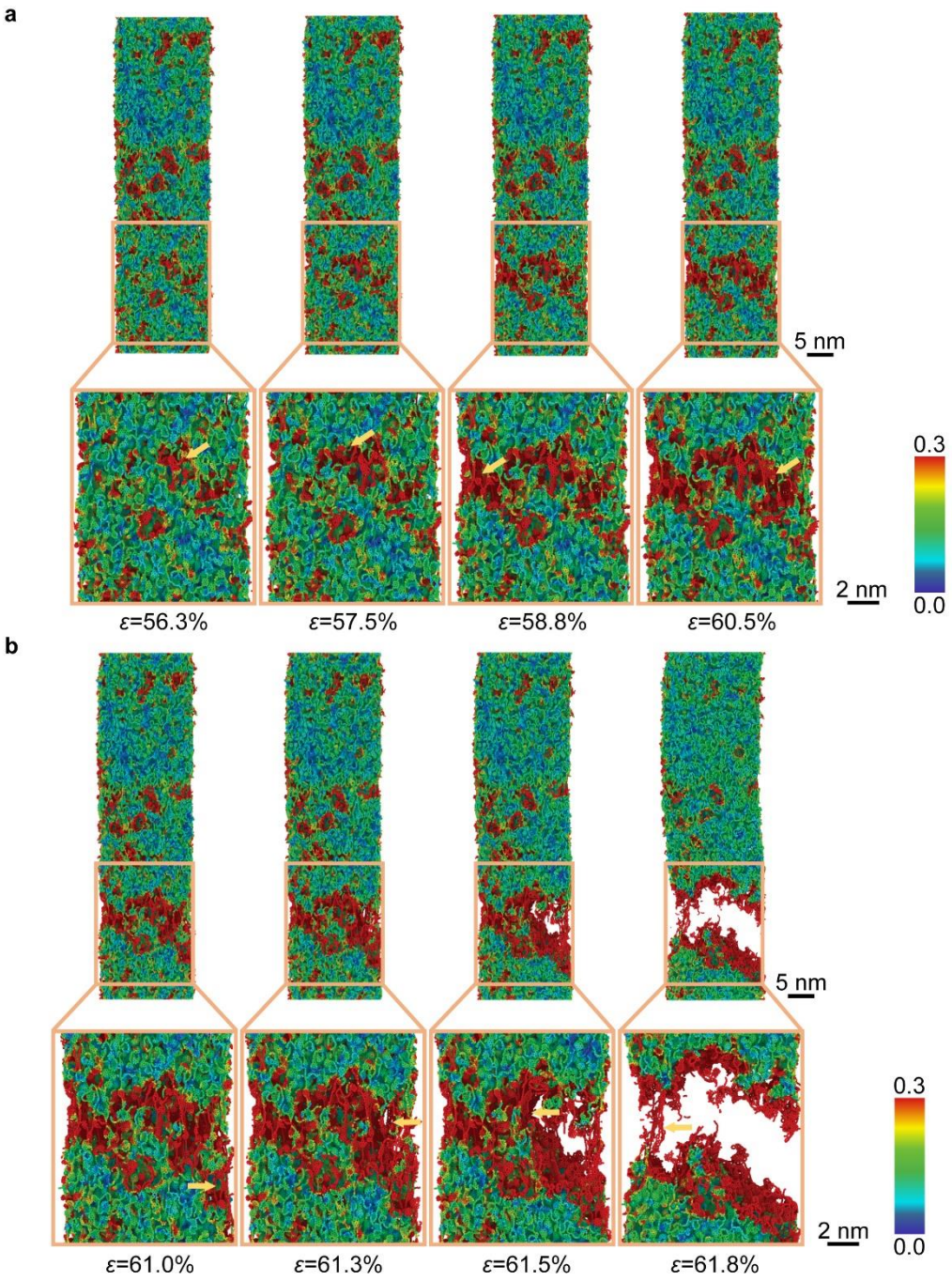

Supplementary Fig. 14 | Fracture mechanisms of pyrolytic carbon nanopillars under uniaxial tension. a, Snapshots of stretched nanopillars at strains of 56.3-60.5%. Nanoscale cavities (indicated by orange arrow) nucleated and grew during stretching, and then merged with each other, leading to formation of nanoscale cracks. **b**, Snapshots of stretched nanopillars at strains of 61.0-61.8%. As the tensile strain increases, nanoscale cracks propagated along a direction normal to tensile direction, resulting in the smooth fracture surface. All atoms in **a** and **b** are colored by atomic von Mises strain.

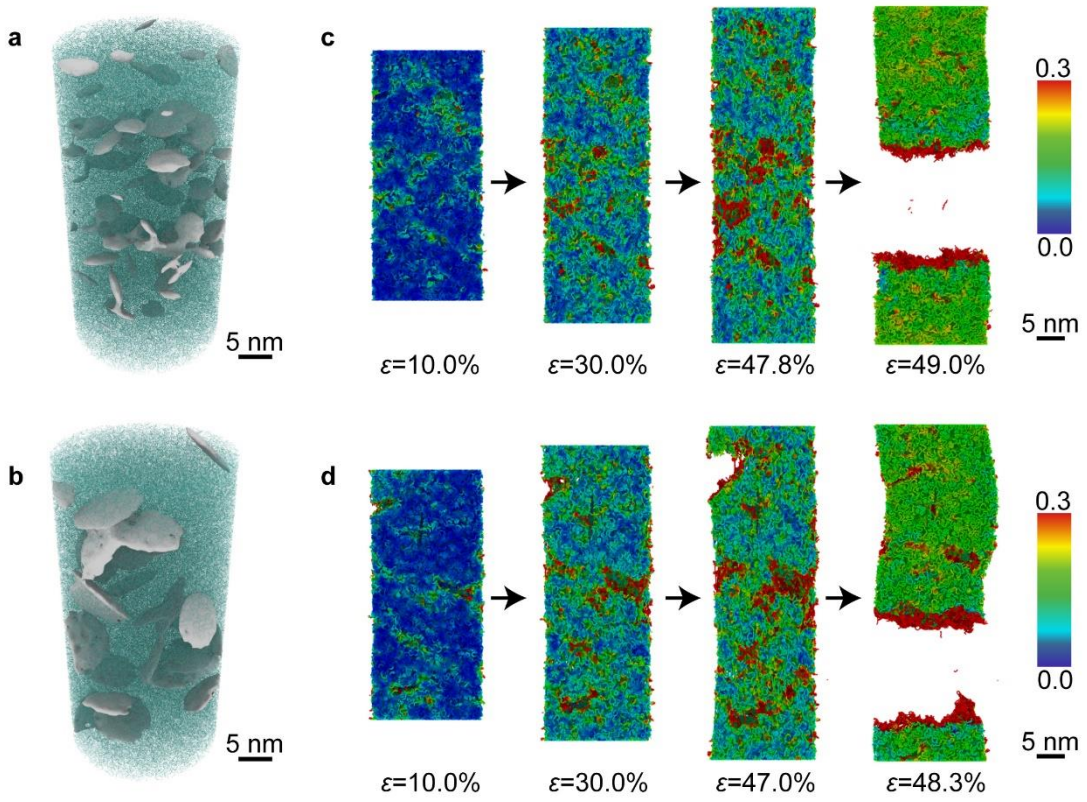

Supplementary Fig. 15 | Effects of initial flaws on tensile strength of pyrolytic carbon pillars. a, **b**, Atomic configurations of simulated samples containing initial cracks with length of 4 nm and 8 nm, respectively. All initial cracks are shown by the white flakes. **c**, **d**, A sequence of snapshots of pillars that contain initial cracks with length of 4 nm and 8 nm, respectively. The failure of both nanopillars always initiated from the growth and extension of pre-existing nanocracks. Both samples after failure exhibit smooth fracture surfaces, showing a brittle fracture mode. All atoms in **c** and **d** are colored by atomic von Mises strain.

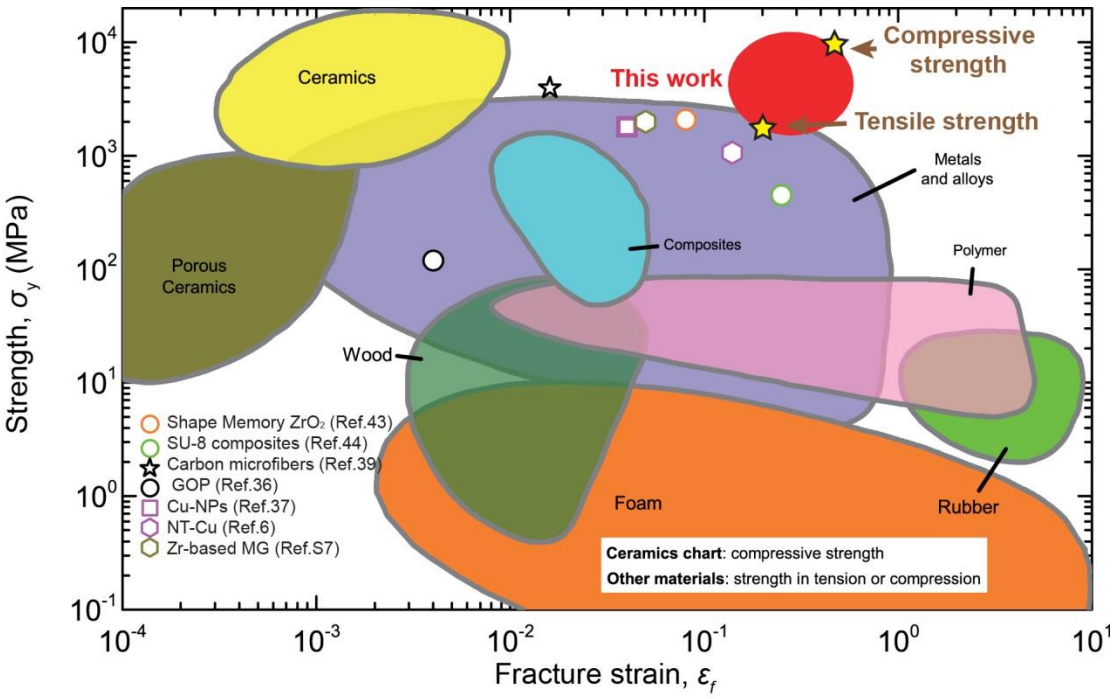

Supplementary Fig. 16 | Summary of strength versus fracture strain for our pyrolytic carbon micropillars and other structural materials. Data collected for structural materials including NT-Cu[6], GOP[36], Cu-NPs[37], carbon microfibers[39], shape memory zirconia[43], SU-8 composites[44], and Zr-based metallic glass nanopillars (MG-NPs)[S7].

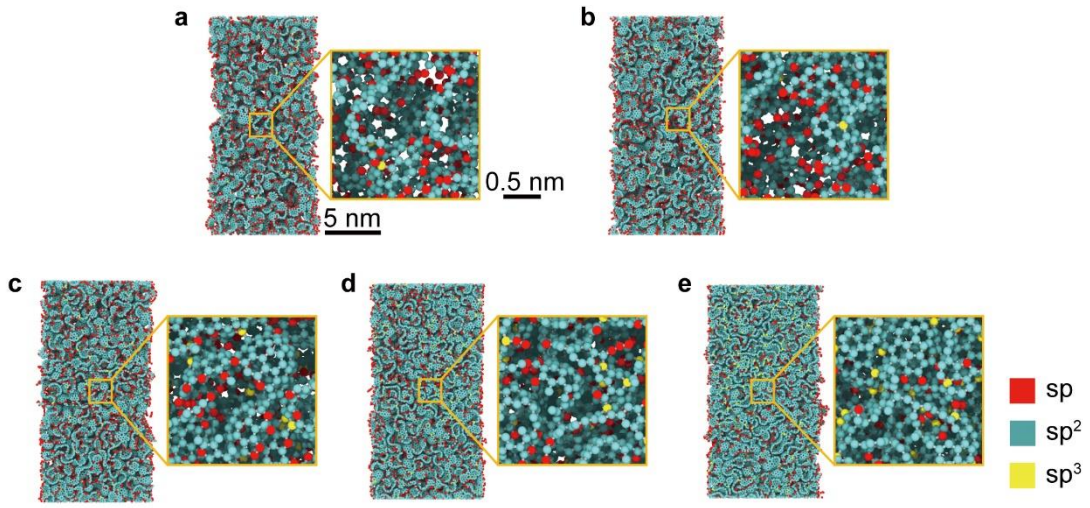

Supplementary Fig. 17 | Atomic configurations of pyrolytic carbon nanopillars with different densities but the same diameter of 10 nm. a-e, Cross-sectional morphology of nanopillars with density varying from 1.0 to 1.8 g/cm^3. Atoms with the sp, sp^2 and sp^3 bonds are painted in red, cyan and yellow, respectively.

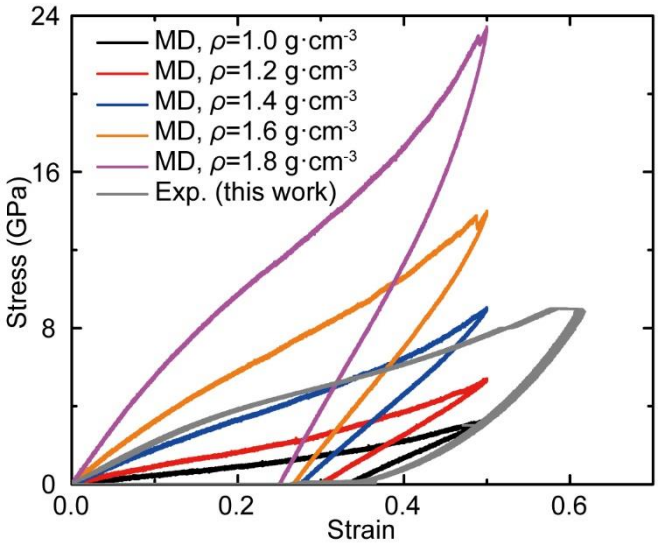

Supplementary Fig. 18 | Simulated compressive stress-strain curves of pyrolytic carbon nanopillars with density varying from 1.0 to 1.8 g/cm^3. For comparison, a typical stress-strain curve from experiments is plotted in this figure. The nanopillars with density of 1.4 g/cm^3 show very similar stress-strain response as the experimental specimens.

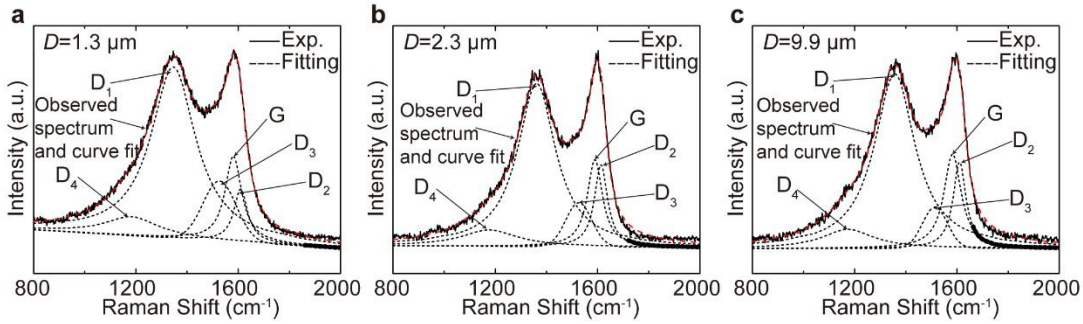

Supplementary Fig. 19 | Raman spectra measured on three samples and associated fitting for *G*, D_1, D_2, D_3 and *D*4 bands. The red dotted line is the sum of *G*, D_1, D_2, D_3 and *D*4 bands.

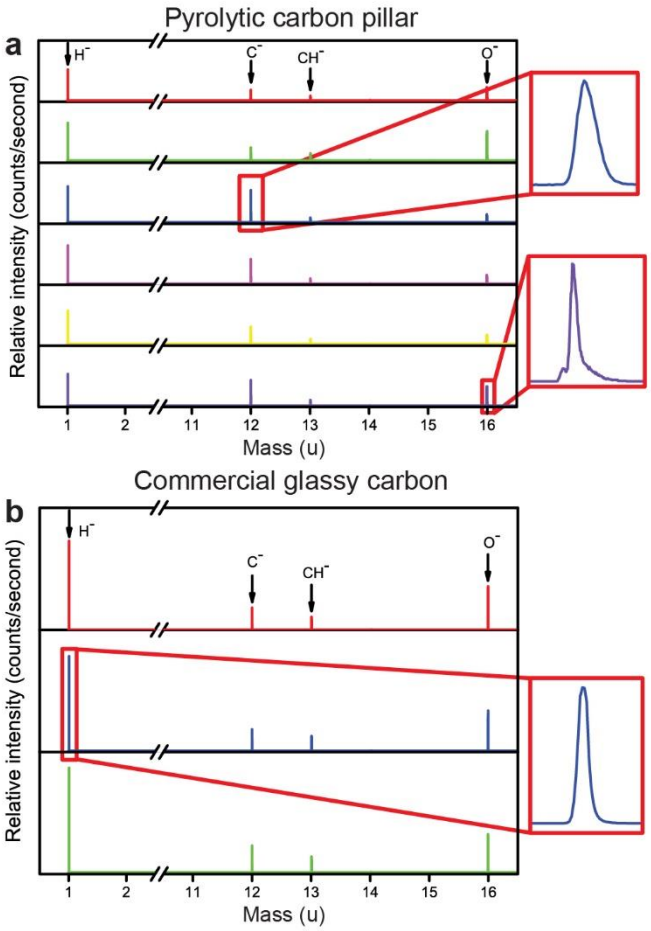

Supplementary Fig. 20 | SIMS spectra measured on pyrolytic carbon micropillars and commercial glassy carbon. a, SIMS spectra of pyrolytic carbon micropillars. **b**, SIMS spectra of commercial glassy carbon, which serves as a reference material to determine the elemental composition of pyrolytic carbon micropillars. Some typical peaks in the SIMS spectra are zoomed in the insets.

Supplementary Table 1. Summary of graphene fragment size evaluated by all Raman spectra measured on samples with different diameters

Diameter D (μm)	Ratio I_D/I_G		Graphene fragment size L (nm)		Laser wavelength λ_l (nm)
	Measured	Average	Calculated	Average	
1.0-1.3	9.27	10.1±0.8	2.1	1.9±0.2	532
	9.41		2.0		
	11.59		1.7		
	9.29		2.1		
	10.21		1.9		
	9.82		2.0		
	10.95		1.8		
1.5-1.8	6.96	8.1±2.1	2.8	2.5±0.5	532
	6.82		2.8		
	8.08		2.4		
	5.78		3.3		
	8.40		2.3		
	12.91		1.5		
	7.70		2.5		
2.0-2.3	7.04	8.0±1.4	2.4	2.2±0.4	514
	6.56		2.6		
	9.02		1.9		
	6.53		2.6		
	8.69		1.9		
	10.13		1.7		
4.4-4.6	5.34	9.0±5.4	3.1	2.3±0.8	514
	8.07		2.1		
	5.47		3.1		
	6.57		2.5		
	19.61		0.9		
9.7-9.9	9.97	10.0±1.6	1.7	1.7±0.2	514
	13.55		1.2		
	9.74		1.7		
	9.14		1.8		
	8.96		1.9		
	8.84		1.9		
12.5-12.7	10.79	9.5±2.2	1.6	1.8±0.3	514
	14.67		1.1		
	8.85		1.9		
	7.18		2.3		
	7.77		2.2		
	9.26		1.8		
	8.40		2.0		
	9.32		1.8		

Captions for Supplementary Videos 1 to 4

Supplementary Video 1 | In situ compression of pyrolytic carbon micropillar with diameter of 2.25 μm. During compression, the micropillar shortened and thickened gradually with increasing compressive strain. A slight tilt sometimes occurred during compression. After unloading, the micropillar shows an elastic recovery of about 10% strain.

Supplementary Video 2 | In situ tension of pyrolytic carbon micropillar with diameter of 1.5 μm. The micropillar was stretched to fail with a smooth fracture surface, at a tensile fracture strain up to about 26%.

Supplementary Video 3 | Atomistic simulation of uniaxial compression on pyrolytic carbon nanopillars with diameter of 20 nm. In the initial compressive stage, the curled graphene layers approached each other, and some graphene layers bent significantly. As the compressive strain increased, a few graphene layers slipped relative to the neighboring layers, leading to abrupt failure under shear. When the compressive strain reached 50%, the sub-nanometer-sized voids tended to close, resulting in densification of the pillars. Slight tilting occurred in the nanopillar due to interlayer slipping and shearing of neighboring graphene layers. During unloading, the nanopillar exhibited a certain level of elastic recovery. The distances between graphene layers increased and the sub-nanometer-sized voids partially reopened.

Supplementary Video 4 | Atomistic simulation of uniaxial tension on pyrolytic carbon nanopillars with diameter of 20 nm. During tension, the curved graphene layers were stretched. A number of nanoscale cavities nucleated, grew and then coalesced, leading to the formation of nanoscale cracks. Eventually, these nanoscale cracks propagated normal to the tensile direction, resulting in a smooth fracture surface.

References for Supplementary Information

S1. Ashby, M. F. & Greer, A. L. Metallic glasses as structural materials. *Scr. Mater.* **54,** 321-326 (2006).

S2. Blackman, L. C., Saunders, G. & Ubbelohde, A. R. Defect structure and properties of pyrolytic carbons. *Proc. R. Soc. Lond. A* **264,** 19-40 (1961).

S3. McEvoy, N. et al. Synthesis and analysis of thin conducting pyrolytic carbon films. *Carbon* **50,** 1216-1226 (2012).

S4. Sebag Bernd, M. G., Braganc, S. R., Heck, N. & Silva FilhoJ, L. C. P. Synthesis of carbon nanostructures by the pyrolysis of wood sawdust in a tubular reactor. *J. Mater. Res. Technol.* **6,** 171-177 (2017).

S5. Sharma, S., Shyam Kumar, C. N., Korvink, J. G. & Kübel, C. Evolution of glassy carbon microstructure: In situ transmission electron microscopy of the pyrolysis process. *Sci. Rep.* **81,** 16282 (2018).

S6. Qu, R. & Zhang, Z. A universal fracture criterion for high-strength materials. *Sci. Rep.* **3,** 1117 (2013).

S7. Jang, D. & Greer, J. R. Transition from a strong-yet-brittle to a stronger-and-ductile state by size reduction of metallic glasses. *Nat. Mater.* **9,** 215-219 (2010).